bioRxiv preprint doi: https://doi.org/10.1101/2020.12.09.418657; this version posted December 10, 2020. The copyright holder for this preprint (which was not certified by peer review) is the author/funder, who has granted bioRxiv a license to display the preprint in perpetuity. It is made available under aCC-BY-NC-ND 4.0 International license.

# Defective oligodendrocyte development and function in an RNA polymerase III mutant leukodystrophic mouse

Emilio Merheb[a], Min-Hui Cui[b,c], Juwen C. DuBois[d], Craig A. Branch[b,c], Maria Gulinello[e], Bridget Shafit-Zagardo[d], Robyn D. Moir[a], Ian M. Willis[a,f,*]

[a] Department of Biochemistry, Albert Einstein College of Medicine, Bronx, NY 10461;
[b] Department of Radiology, Albert Einstein College of Medicine, Bronx, NY 10461;
[c] Gruss Magnetic Resonance Research Center, Albert Einstein College of Medicine, Bronx, NY 10461;
[d] Department of Pathology, Albert Einstein College of Medicine, Bronx, NY 10461;
[e] Department of Neuroscience, Albert Einstein College of Medicine, Bronx, NY 10461;
[f] Department of Systems and Computational Biology, Albert Einstein College of Medicine, Bronx, NY 10461

* Corresponding author: Ian M Willis.
**Email:** ian.willis@einsteinmed.org

**Author Contributions:** R.D.M. and I.M.W. conceived the study. E.M acquired and analyzed data. J.C.D contributed to the immunohistochemistry. M.G. designed and supervised behavioral studies and reviewed the statistical analysis. M-H.C. performed and analyzed the MRI, DTI and MRS data and designed these experiments together with C.A.B. B.S-Z. contributed to the design and interpretation of immunohistochemistry and TEM data. E.M and I.M.W wrote the manuscript with contributions from the other authors. All authors read and approved the final version of the manuscript.

**Keywords:** RNA polymerase III; leukodystrophy; oligodendrocyte; hypomyelination

bioRxiv preprint doi: https://doi.org/10.1101/2020.12.09.418657; this version posted December 10, 2020. The copyright holder for this preprint (which was not certified by peer review) is the author/funder, who has granted bioRxiv a license to display the preprint in perpetuity. It is made available under aCC-BY-NC-ND 4.0 International license.

**Abstract**

RNA polymerase (Pol) III synthesizes abundant short non-coding RNAs that have essential functions in protein synthesis, secretion and other processes. Despite the ubiquitous functions of these RNAs, mutations in Pol III subunits cause Pol III-related leukodystrophy, an early-onset neurodegenerative disease. The basis of this neural sensitivity and the mechanisms of disease pathogenesis are unknown. Here we show that mice expressing pathogenic mutations in the largest Pol III subunit, *Polr3a,* specifically in Olig2-expressing cells, have impaired growth, neurobehavioral deficits and hypomyelination in multiple regions of the brain and spinal cord. We identify two mechanisms of disease pathogenesis within the oligodendrocyte (OL) lineage; a differentiation defect of oligodendrocyte precursor cells reduces the number of mature myelinating OLs and an intrinsic myelination defect in mature OLs impairs myelin deposition. Thus, we reveal cell-specific roles for Pol III in the normal development and function of oligodendrocytes.

bioRxiv preprint doi: https://doi.org/10.1101/2020.12.09.418657; this version posted December 10, 2020. The copyright holder for this preprint (which was not certified by peer review) is the author/funder, who has granted bioRxiv a license to display the preprint in perpetuity. It is made available under aCC-BY-NC-ND 4.0 International license.

## Introduction

Leukodystrophies constitute a group of genetically heterogeneous inherited diseases that affect myelin sheath production and/or function in the central nervous system (CNS) (1). They include disorders such as Pelizaeus-Merzbacher disease, where the causal mutation involves a myelin-specific gene, and many other disorders where the causal mutations affect gene functions that are required more broadly (1). With the increasing functional diversity of leukodystrophy-associated genes, it has become apparent that these diseases are not restricted to cells of the oligodendrocyte lineage, which ultimately produce myelin, but may involve astrocytes, microglia and/or neurons (2). RNA polymerase (Pol) III-related leukodystrophy, an autosomal recessive disorder, is the second most prevalent leukodystrophy (3) and was identified when five initially distinct syndromes with overlapping clinical and radiological features were found to have a common molecular basis (4-6). Pol III-related leukodystrophy is typically a hypomyelinating disorder and is known for its high phenotypic variability (4-10). Patients are diagnosed between birth and adolescence with neurological and non-neurological deficits, and are classified according to distinct brain MRI features and confirmed by sequencing (11). Neurological deficits include developmental delay with a progressive decline in cognitive and motor function, ataxia, cerebellar atrophy and a hypoplastic corpus callosum. Non-neurological deficits may include hypodontia, myopia and endocrine abnormalities such as hypogonadotropic hypogonadism and growth hormone deficiency (8). An understanding of the disease mechanisms underlying these clinical characteristics is currently lacking.

Pol III is the largest eukaryotic RNA polymerase and is composed of seventeen subunits. Ten of these subunits are unique to Pol III, five are common to all three nuclear

bioRxiv preprint doi: https://doi.org/10.1101/2020.12.09.418657; this version posted December 10, 2020. The copyright holder for this preprint (which was not certified by peer review) is the author/funder, who has granted bioRxiv a license to display the preprint in perpetuity. It is made available under aCC-BY-NC-ND 4.0 International license.

RNA polymerases and the remaining two subunits are shared with Pol I. The enzyme transcribes abundant non-coding RNAs such as tRNA, 5S rRNA, U6 snRNA and 7SL RNA that are involved in essential cellular processes including protein synthesis, RNA processing/splicing and protein secretion among others (12-14). Pol III-related leukodystrophy mutations were initially identified in the two largest subunits, *Polr3a* and *Polr3b,* which form the catalytic core of the enzyme. Subsequently, disease-causing mutations have been found in three other subunits, *Polr1c*, *Polr3k* and *Polr3gl* (15-17). In most cases, biallelic, compound heterozygous mutations have been reported although several homozygous mutations have also been identified. Mapping of >100 Pol III-related leukodystrophy disease mutations on the cryo-EM structure of human Pol III suggests a variety of molecular defects from disrupted subunit folding and subunit-subunit interactions that likely impact enzyme assembly (15) to impaired functions involving structural elements important for catalysis and surface-exposed sites (18, 19). How these hypomorphic alleles alter the Pol III transcriptome to cause disease is a major unanswered question. Studies with patient-derived fibroblasts and other cell-based systems suggest a range of possible effects from a global reduction in translation due to decreased synthesis of tRNA and 5S rRNA to more limited or even gene-specific effects (e.g. reduced BC200 and 7SL RNAs) (16, 20, 21). However, the molecular mechanisms of pathogenesis remain poorly characterized and further progress is significantly limited by the absence of an animal model of the disease.

In this study, we report the characterization of a mouse model of Pol III-related leukodystrophy, the first to exhibit features of the disease found in patients. Conditional knock-in of a *Polr3a* double mutant allele in Olig2-expressing cells results in developmental delay in neonates and cognitive, sensory and fine sensorimotor deficits in

bioRxiv preprint doi: https://doi.org/10.1101/2020.12.09.418657; this version posted December 10, 2020. The copyright holder for this preprint (which was not certified by peer review) is the author/funder, who has granted bioRxiv a license to display the preprint in perpetuity. It is made available under aCC-BY-NC-ND 4.0 International license.

adult mice. These neurobehavioral phenotypes are consistent with hypomyelination of multiple regions in the CNS as revealed by magnetic resonance and diffusion tensor imaging, immunohistochemistry and electron microscopy. Along with an analysis of oligodendrocyte cell populations and specific protein markers, we identify two mechanisms that contribute to disease pathogenesis: Defective differentiation of oligodendrocyte precursor cells (OPCs) and defective function of mature oligodendrocytes (OLs). Together, these defects result in impaired oligodendrogenesis and myelination. The work highlights the importance of Pol III transcription for normal oligodendrocyte development and function and provides a model for further exploration of the role of Pol III in diseases of the CNS and other tissues.

## Results

### A neural-specific defect in *Polr3a* leads to reduced growth and delayed postnatal development.

We engineered mice with whole body and conditional knock-in mutations (W671R/G672E) at adjacent positions in *Polr3a*. Homozygosity for either mutation causes Pol III-related leukodystrophy in humans (8). However, mice that are homozygous or hemizygous for the G672E mutation alone have no apparent phenotype (22, 23). The corresponding mutation in the homologous yeast subunit also had no phenotype (24). By contrast, mutation of both sites in the yeast *Polr3a* homolog results in temperature-sensitive growth and defects in Pol III transcription (24). Mice that are heterozygous for the whole body double mutant knock-in (*Polr3a*$^{KI/+}$) have a normal body weight compared to WT mice (Fig. S1 A and B) and express WT and mutant *Polr3a* mRNAs at approximately equal levels (Fig. S1 C). POLR3A protein and total tRNA levels are unchanged in the brain and northern blotting for a precursor tRNA that serves as an

bioRxiv preprint doi: https://doi.org/10.1101/2020.12.09.418657; this version posted December 10, 2020. The copyright holder for this preprint (which was not certified by peer review) is the author/funder, who has granted bioRxiv a license to display the preprint in perpetuity. It is made available under aCC-BY-NC-ND 4.0 International license.

indicator of Pol III transcription also showed no change (Fig. S1 E-J). Nonetheless, homozygosity for the whole body knock-in (*Polr3a*$^{KI/KI}$) was lethal prior to embryonic day 12.5 (E12.5) (Fig. S1 D). Since the major clinical feature of Pol III-related leukodystrophy is hypomyelination (4-8), we used an *Olig2*-Cre driver and conditional *Polr3a* mutant knock-in (*Polr3a*$^{cKI/cKI}$) mice in an effort to bypass embryonic lethality and investigate the effects of the mutation on myelination. Olig2, a CNS-specific basic helix-loop-helix transcription factor, becomes active at E11.5 and is expressed throughout the oligodendrocyte lineage as well as in a subset of motor neurons and GFAP-negative astrocytes (25-27). *Olig2*$^{Cre+/-}$ *Polr3a*$^{cKI/cKI}$ mice (hereafter referred to as Polr3a-cKI mice) are viable and exhibit recombination frequencies of ~83% in females and ~88% in males based on FACS analysis of O4-positive oligodendrocytes from brain homogenates of mice expressing a dual tdTomato-EGFP reporter (Fig. S2).

Pol III-related leukodystrophy patients are often diagnosed at an early stage in development (early childhood to adolescence), therefore we investigated the mice for phenotypes as neonates (P1-P21), adolescents (3-5 weeks of age) and adults (≥8 weeks of age). For neonates, we tracked body weight and monitored the acquisition of developmental milestones that serve as indicators of neurodevelopmental disorders. Polr3a-cKI neonates of both sexes have significantly lower body weights than the corresponding WT mice (Fig. 1 A and B). This difference is more pronounced in males and increases over time from P5 to P21 in contrast to females which maintain a relatively constant and smaller body weight difference. Male and female Polr3a-cKI mice also show a delay in achieving developmental milestones that reflect deficits in body righting mechanisms, strength, coordination, locomotion and the extinguishing of pivoting behavior (Fig. 1 C and D) (28). Notably, impaired growth and developmental

bioRxiv preprint doi: https://doi.org/10.1101/2020.12.09.418657; this version posted December 10, 2020. The copyright holder for this preprint (which was not certified by peer review) is the author/funder, who has granted bioRxiv a license to display the preprint in perpetuity. It is made available under aCC-BY-NC-ND 4.0 International license.

delay is also seen in patients with Pol III-related leukodystrophy (8).

**Impaired growth and myelination in adolescent and adult Polr3a-cKI mice.**

In humans and in rodents, postnatal growth impairment (e.g. due to malnutrition) can be followed by a period of catch-up growth. However, the body weight difference of Polr3a-cKI mice was maintained in males and enhanced in females between 3 and 5 weeks of age (Fig. 1 G and J). These changes correlated with a smaller body size and lower brain weight throughout adolescence (Fig. 1 E, F, H, I, K and L). Differences in body weight and size were also evident in adult animals at 12 and 16 weeks of age (Fig. S3 A-D).

To investigate myelin deposition in the CNS we harvested brains and spinal cords from adolescent and adult WT and Polr3a-cKI mice (Fig. 1 F) and performed immunohistochemistry targeting the lipid and protein components of myelin. In coronal sections, Luxol fast blue (LFB) staining of the phospholipid portion of myelin revealed reduced intensity in the corpus callosum splenium, hippocampus and cerebral cortex of adolescent Polr3a-cKI mice (Fig. 2 A-D). Similar observations were made for LFB staining of these regions in adult mice. Additionally, FluoroMyelin staining of the total lipid portion of myelin was reduced in the corpus callosum genu (Fig. S3 G and K). Comparable findings were obtained for myelin-specific proteins: myelin basic protein (MBP) staining of coronal sections from adolescent and adult mouse brain was reduced in the corpus callosum splenium, hippocampus and the cerebral cortex and myelin-associated glycoprotein (MAG) staining was decreased in the corpus callosum genu (Fig. 2 E-H and Fig. S3 F, J, H and L). Changes in myelination were also apparent in the spinal cord where LFB and MBP staining of the ventral and dorsal horns was reduced and there was a reduction in the size of the white matter tract due to the

bioRxiv preprint doi: https://doi.org/10.1101/2020.12.09.418657; this version posted December 10, 2020. The copyright holder for this preprint (which was not certified by peer review) is the author/funder, who has granted bioRxiv a license to display the preprint in perpetuity. It is made available under aCC-BY-NC-ND 4.0 International license.

projection of the ventral horns into the ventrolateral funiculus (Fig. 2 I-L). Surprisingly, given the important role of the cerebellum in motor control and the frequent ataxia reported in Pol III-related leukodystrophy patients (8), LFB and MBP staining in sagittal sections of the cerebellum did not show any difference compared to WT (Fig. 2 M-P). Additionally, we counted Purkinje cells, which express Olig2 (25), after Nissl staining and found no difference (Fig. S3 M and N). Altogether the immunohistochemical data reveal impaired myelination in distinct anatomical regions in the cerebrum and the spinal cord but no apparent changes in the cerebellum.

**Adult Polr3a-cKI mice exhibit multiple neurobehavioral deficits.**

Pol III-related leukodystrophy patients present with neurological deficits including impaired cognitive and motor functions (8). To determine whether neurological deficits are present in Polr3a-cKI mice, we performed a battery of behavioral tests. Initially, we utilized a behavioral spectrometer with video tracking and pattern recognition analysis to quantify numerous home cage-like locomotion and repetitive behaviors. No significant differences were observed although mutant male mice showed a trend towards a shorter center track length suggesting an anxiety-like behavior (Fig. S4 A-F). However, further investigation of this behavior using an elevated plus-maze did not reveal any difference compared to WT mice (Fig. S4 I). Cognitive functions involving visual and spatial memory were assessed by object recognition (OR) and object placement (OP) tests, respectively, using a preference score cutoff of 55 (time exploring a new object or location/total time of exploration x 100) to demonstrate the animals' inherent preference for novelty. With this as the criterion, 90-100% of male and female WT mice scored above the cutoff on both the OP and OR tests. In contrast, >60% of male and ~80% of female Polr3a-cKI mice scored below the cutoff in OP, i.e. failed to differentiate between

bioRxiv preprint doi: https://doi.org/10.1101/2020.12.09.418657; this version posted December 10, 2020. The copyright holder for this preprint (which was not certified by peer review) is the author/funder, who has granted bioRxiv a license to display the preprint in perpetuity. It is made available under aCC-BY-NC-ND 4.0 International license.

familiar and novel locations (Fig. 3 A and B) and ~60% of female Polr3a-cKI mice failed to differentiate between familiar and novel objects in OR (Fig. S4 H). These data point to impaired cognitive functions involving the hippocampus and other brain regions (29).

The Hargreaves test was used to investigate the reflex response to thermal sensation. Both WT and Polr3a-cKI mice showed increased latency for hind paw withdrawal as a function of stimulus intensity (Fig. 3 C and D). However, the relative response was significantly delayed for Polr3a-cKI mice at lower intensities for males and at all intensities for females, suggesting an impaired sensation and reflex response. Auditory and sensorimotor reflexes were investigated using an acoustic startle test. Male Polr3a-cKI mice exhibited a significant reduction in the magnitude of the startle reflex at all stimulus intensities whereas the corresponding female mice exhibited a trend at lower stimuli and a significant reduction at 115 dB (Fig. 3 G and H). Given the differences observed for male and female mice at 115 dB, we examined the latency to respond at this stimulus intensity and found a significant delay, relative to WT, for both sexes to elicit a startle reflex (Fig. 3 I). Together, these data indicate that Polr3a-cKI mice have impaired auditory and thermal sensorimotor reflexes.

To determine if the ataxic phenotype observed in patients is evident in the mice, balance beam and rotarod experiments were used to assess gross motor coordination and motor memory. The number of slips made by Polr3a-cKI mice on four balance beams of varying diameter was not statistically different from WT mice (Fig. 3 J and K). Similarly, Polr3a-cKI mice exhibited no difference in latency to fall from an accelerating rod compared to WT mice using protocols to assess short-term or long-term memory (Fig. S4 J and K). The lack of any difference in these tests was consistent in both sexes

bioRxiv preprint doi: https://doi.org/10.1101/2020.12.09.418657; this version posted December 10, 2020. The copyright holder for this preprint (which was not certified by peer review) is the author/funder, who has granted bioRxiv a license to display the preprint in perpetuity. It is made available under aCC-BY-NC-ND 4.0 International license.

suggesting an absence of gross motor coordination and motor memory dysfunction. In contrast, significant differences in fine sensorimotor function were revealed using a tape removal test. Polr3a-cKI mice showed a significant delay in active removal latency over two consecutive days (Fig. 3 E and F). The delay was present for both days and in both sexes suggesting impaired fine sensorimotor function. Thus, along with impaired growth and hypomyelination, these data indicate that adult Polr3a-cKI mice exhibit deficits in cognitive, sensory, fine sensorimotor, auditory and reflex functions compared to WT mice.

**Impaired myelin integrity revealed by magnetic resonance and diffusion tensor imaging.**

Quantitative magnetic resonance imaging (MRI) is an important diagnostic tool for detecting and monitoring lesions, inflammation and white matter changes in the CNS caused by traumatic injury and a wide range of neurodegenerative diseases (30). In patients with Pol III-related leukodystrophy, diffuse hypomyelination is typically identified by MRI as hyperintensity in T2-weighted images of white matter regions (4, 5, 7, 8). We performed brain MRIs on adult WT and Polr3a-cKI mice and determined T1 and T2 relaxation times for different white and grey matter regions (Table 1 and Fig. S5 A). In agreement with the immunohistochemical findings for adolescent and adult Polr3a-cKI mice, T2 relaxation times increased in the corpus callosum consistent with hypomyelination. To further explore the myelination defect in the mice, we utilized diffusion tensor imaging (DTI), a high-resolution methodology that provides microstructural information about white matter fibers based on the diffusion properties of water (31). Parallel bundles of axons promote water diffusion along their length (axial diffusivity, AD) and restrict it perpendicular to the tract (radial diffusivity, RD) resulting in

bioRxiv preprint doi: https://doi.org/10.1101/2020.12.09.418657; this version posted December 10, 2020. The copyright holder for this preprint (which was not certified by peer review) is the author/funder, who has granted bioRxiv a license to display the preprint in perpetuity. It is made available under aCC-BY-NC-ND 4.0 International license.

high fractional anisotropy (FA). Interestingly, in Polr3a-cKI mice, FA was reduced significantly in the anterior commissure, corpus callosum genu and splenium and the optic tract due to increased RD in the absence of effects on AD (Table 2 and Fig. S5 B). These data suggest a myelin deficiency in these regions, comparable to those reported in Shiverer mice (32). In contrast, the optic nerve showed no change in FA but reduced RD, AD and mean diffusivity (MD). These changes recapitulate observations made in a mouse model of retinal ischemia that were interpreted to represent axonal degeneration and myelin fragmentation in the optic nerve (33). The DTI data also revealed high but unchanged FA in structures of the cerebellum and the pons with no changes in diffusivities (Fig. S5 B and C) suggesting that myelin integrity in these regions is not altered, consistent with immunohistochemical and gross motor behavioral data.

Magnetic resonance spectroscopy (MRS) in leukodystrophy patients has previously identified metabolic alterations in N-acetylaspartate and myo-inositol (Ins). Decreased N-acetylaspartate has been linked to neuronal loss while elevated Ins has been linked to oligodendrogliosis and impaired myelination and/or myelin integrity (34-36). We performed MRS on the hippocampus given the immunohistochemical and cognitive deficits associated with this region (Fig. 2 A and C and Fig. 3 A and B). The levels of NAA and seven other metabolites were unchanged. However, the level of Ins in Polr3a-cKI mice was increased consistent with a myelination defect (Table S1).

**Ultrastructural analysis reveals defects in myelination.**

Transmission electron microscopy (TEM) was performed on the corpus callosum to directly examine axonal myelination in the mice. Images were collected at multiple magnifications (Fig. 4, A-D) for the quantitation of myelinated axon size (cross-sectional

bioRxiv preprint doi: https://doi.org/10.1101/2020.12.09.418657; this version posted December 10, 2020. The copyright holder for this preprint (which was not certified by peer review) is the author/funder, who has granted bioRxiv a license to display the preprint in perpetuity. It is made available under aCC-BY-NC-ND 4.0 International license.

area), relative myelin thickness (i.e. g-ratio, axon radius/axon plus myelin radius) and the number of unmyelinated axons per unit volume. Myelin sheath thickness of Polr3a-cKI mice was substantially reduced compared to WT mice as indicated by the higher average g-ratio (Fig. 4 E). Reduced myelin thickness was observed across a range of axon calibers as seen from a linear fit of g-ratios versus axon diameter (Fig. 4 H). These results reveal an intrinsic defect in the capacity of mature oligodendrocytes to produce a myelin sheath of normal thickness in the mutant mice. Additionally, myelinated axons in Polr3a-cKI mice show a narrower distribution of axon caliber with both small and large diameter axons underrepresented (Fig. 4 H) and a reduction in the average cross-sectional area of axons in myelinated fibers (Fig. 4 F). The reduction in axonal size is indicative of impaired growth of white matter tracts as seen in a number of neurodegenerative disorders such as Angelman syndrome (37). There was also a marked increase in the number of unmyelinated axons exhibiting cross-sectional areas greater than the smallest myelinated axons observed in WT mice (Fig. 4 G). The increase in unmyelinated axons suggests that Polr3a-cKI mice may have fewer mature oligodendrocytes and/or fewer myelinating processes per mature oligodendrocyte (38).

We also examined TEM images of the dentate gyrus region of the hippocampus (Fig. S6). Although variability in axon orientation relative to the sectioning plane limits the morphometric analysis, an examination of multiple images supports the qualitative conclusion that the number of myelinated axons and myelin thickness is reduced in this region, consistent with the findings in the corpus callosum (Fig. 4).

**Impaired oligodendrogenesis in the brain of adolescent and adult Polr3a-cKI mice.**

bioRxiv preprint doi: https://doi.org/10.1101/2020.12.09.418657; this version posted December 10, 2020. The copyright holder for this preprint (which was not certified by peer review) is the author/funder, who has granted bioRxiv a license to display the preprint in perpetuity. It is made available under aCC-BY-NC-ND 4.0 International license.

The production of mature myelinating oligodendrocytes from oligodendrocyte precursor cells begins at birth, reaches a peak during postnatal development (~P14-P28) and then declines, but continues into adulthood where newly formed OLs play multiple important roles including neuronal activity-based myelination during task-learning (39). Ultrastructure analysis of Polr3a-cKI mice suggested that, in addition to the diminished function of myelinating oligodendrocytes, myelination might be further limited by reductions in the number of mature oligodendrocytes. To examine this possibility, we used flow cytometry to quantify OPCs and mature oligodendrocytes (OLs) in single-cell suspensions of dissociated whole brain (40). As a gating strategy, we utilized Alexa Fluor 647-conjugated antibodies against O4, a marker of OPCs, and PE-Cy7-conjugated antibodies against MOG, a marker of terminally differentiated myelinating oligodendrocytes (OLs) (40). Additionally, we used mice containing the dual tdTomato-EGFP reporter and gated EGFP-expressing cells in Polr3a-cKI samples so that only oligodendrocyte lineage cells that had undergone Cre-mediated recombination would be counted (Fig. S7). Representative scatter plots of samples from adolescent female mice show the cell populations, including O4 and MOG double-positive pre-myelinating oligodendrocytes (40) (Fig. 5 A). From these data we calculated the fractional representation of the three oligodendrocyte populations (Fig. 5 B-E). The results for adolescent and adult mice of both sexes show reduced numbers of MOG-only expressing OLs. In addition, there was a significant reduction in double-positive pre-OLs among adolescent male Polr3a-cKI mice and a similar trend among adolescent female mice that, in both cases, was absent in the adults. In keeping with the lower number of OLs in Polr3a-cKI mice, this observation is consistent with a defect in oligodendrogenesis.

bioRxiv preprint doi: https://doi.org/10.1101/2020.12.09.418657; this version posted December 10, 2020. The copyright holder for this preprint (which was not certified by peer review) is the author/funder, who has granted bioRxiv a license to display the preprint in perpetuity. It is made available under aCC-BY-NC-ND 4.0 International license.

To validate these findings, we performed western blot analyses to assess changes in the levels of proteins that serve as markers for OPCs (PDGFR-α), OLs (CC1) and myelin (MOG) (41). Given the apparent absence of myelination defects in the cerebellum, protein extracts were prepared from both the cerebrum and cerebellum dissected from adolescent and adult mice. Quantitation and normalization of band intensities using either Ponceau stained membranes or vinculin signals showed a significant decrease in MOG and CC1 in the cerebrum of adolescent and adult Polr3a-cKI mice with no difference in the cerebellum (Fig. 6 A-C and Fig. S8 A-C). PDGFR-α levels were increased in the cerebrum of adolescent but not adult Polr3a-cKI mice with no difference in the cerebellum (Fig. 6 D and Fig. S8 D). Finally, since apoptosis of pre-myelinating OLs is known to control OL maturation and myelination (41, 42), we looked for evidence of caspase 3 activation by western blotting but found none (Fig. 6 A and E and Fig. S8 A and E). Together, the findings from western analysis and flow cytometry support a defect in oligodendrocyte differentiation leading to reduced numbers of mature OLs in adolescent and adult mice.

## Discussion

Previous efforts to develop a mouse model of Pol III-related leukodystrophy have been unsuccessful, either because a known homozygous disease-causing *Polr3a* G672E mutation had no phenotype in mice or because homozygosity for one mutation (*Polr3b* R103H) from a compound heterozygous variant was embryonic lethal (22, 23). We reasoned that enhancing the defect of the *Polr3a* G672E mutation might produce a viable disease model. However, homozygosity for the *Polr3a* W671R/G672E mutation, a construct informed by patient data and by structure-function studies in yeast (8, 24), resulted in embryonic lethality prior to E12.5. In other studies, early embryonic lethality

bioRxiv preprint doi: https://doi.org/10.1101/2020.12.09.418657; this version posted December 10, 2020. The copyright holder for this preprint (which was not certified by peer review) is the author/funder, who has granted bioRxiv a license to display the preprint in perpetuity. It is made available under aCC-BY-NC-ND 4.0 International license.

between E3.5 and E6.5 has been documented for deletions of the Pol III transcription factor *Brf1* (43) and for *Polr3g*, a Pol III subunit isoform that is expressed in mouse embryonic stem cells at a level six-fold higher than its *Polr3gl* paralog (44). This implies that viability during embryonic development requires >15% of wild-type Pol III activity in the critical period of rapid growth prior to gastrulation. Consistent with this, biochemical studies on a yeast Pol III mutant corresponding to *Polr3a* W671R/G672E, show that the mutations reduce Pol III activity to approximately one-third of the wild-type level (24). Since mice that are homozygous or hemizygous for the *Polr3a* G672E mutation appear normal up to at least twelve months of age (22), there appears to be a narrow functional window in mice versus humans for *Polr3a* mutations to both support embryogenesis and generate leukodystrophy phenotypes.

In mice, the production of OPCs begins around E12.5 with the first myelin-expressing OLs appearing just before birth (39). Given the timing of oligodendrogenesis relative to the rapid early cell divisions that precede gastrulation, we hypothesized that a conditional knock-in of the *Polr3a* W671R/G672E mutation in oligodendrocytes might support viability and exhibit disease phenotypes. Indeed, Polr3a-cKI mice display multiple phenotypes that parallel those seen in typical Pol III-related leukodystrophy patients. The developmental delay in neonates and the growth rate reduction that continues through adulthood are notable examples (8). The existence of a growth rate phenotype in a Pol III hypomorph that is restricted to the Olig2 lineage is intriguing and suggests a cell non-autonomous effect. Interestingly, the short stature of many Pol III-leukodystrophy patients correlates with a growth hormone deficiency among a number of tested patients (8, 45). How this reduction in growth hormone is achieved is not known. However, the patient data together with our findings suggest a role for oligodendrocytes

bioRxiv preprint doi: https://doi.org/10.1101/2020.12.09.418657; this version posted December 10, 2020. The copyright holder for this preprint (which was not certified by peer review) is the author/funder, who has granted bioRxiv a license to display the preprint in perpetuity. It is made available under aCC-BY-NC-ND 4.0 International license.

in the regulation of growth hormone production by the pituitary gland and/or glia control of the hypothalamic-pituitary axis. Such effects could also account for the observed hypogonadotropic hypogonadism of Pol III-related leukodystrophy patients (46).

Polr3a-cKI mice exhibit impairments in cognition, auditory and thermal sensorimotor reflexes and fine sensorimotor function consistent with hypomyelination in multiple regions of the cerebrum (hippocampus, cortex, corpus callosum) and the spinal cord (47). Diffuse hypomyelination, assessed by MRI, is also a common phenotype of Pol III-related leukodystrophy patients and typically includes regions in the cerebrum, notably the corpus callosum, as well as the cerebellum where it is often associated with cerebellar atrophy and gross motor defects (8). Interestingly, even though Olig2 is expressed throughout the oligodendrocyte lineage, Polr3a-cKI mice showed no signs of hypomyelination in the cerebellum by histology, DTI or western blotting and did not exhibit a gross motor defect or ataxia. The basis of this differential hypomyelination in the cerebrum versus the cerebellum is unknown. However, it is well-known that the survival and differentiation of OPCs along with the function of OLs and the maintenance of myelin is dependent on the actions of neighboring astrocytes and microglia and on the ensheathed axons (2). These observations raise the possibility that cell-intrinsic changes in cerebellar oligodendrocytes are suppressed in our model by cell extrinsic factors. A possible mechanism is the ability of astrocyte-derived lipids to supplement lipid synthesis in OLs (48). Whatever the mechanism, the data suggest that targeting the *Polr3a* mutation to additional cell types in the CNS is likely to provoke hypomyelination in the cerebellum and lead to a more severe disease model.

bioRxiv preprint doi: https://doi.org/10.1101/2020.12.09.418657; this version posted December 10, 2020. The copyright holder for this preprint (which was not certified by peer review) is the author/funder, who has granted bioRxiv a license to display the preprint in perpetuity. It is made available under aCC-BY-NC-ND 4.0 International license.

Our study reveals two distinct deficits within the oligodendrocyte lineage of Polr3a-cKI mice that contribute in different ways to changes in myelination: (i) A defect in differentiation that reduces the number of mature myelinating OLs and (ii) a diminished capacity for myelin deposition by mature OLs that reduces myelin thickness on axons of all sizes. The finding that a defect in Pol III function can determine cell fate and/or differentiation is mechanistically novel and has not previously been reported in neural tissues. Chen et al showed that either genetic or chemical inhibition of Pol III transcription promoted adipogenesis in NIH 3T3-L1 cells and in primary cells cultured from the stromal vascular fraction of inguinal fat pads (49). Conversely, increased Pol III transcription in mouse embryonic stem cells, through knockdown of its master negative regulator, MAF1, inhibited the formation of the mesodermal germ layer and the terminal differentiation of mesoderm into adipocytes. In the context of these studies, our findings support the capacity of Pol III transcription to affect differentiation in the oligodendrocyte lineage and show that such effects are not limited to cells in vitro but can be achieved in an animal model. Thus, the combination of a defect in oligodendrogenesis with an intrinsic myelination defect in OLs provide a basis for the observed neurobehavioral deficits.

In summary, we describe the first animal model of Pol III-related leukodystrophy that recapitulates clinical features of the disease. The complexity of the disease and the ability of Pol III mutations to broadly impact cellular function is demonstrated by the identification of two mechanistically distinct defects within the oligodendrocyte lineage that together lead to myelination, neurobehavioral and other deficits. Further studies of the mice will enhance our molecular understanding of disease pathogenesis and enable

bioRxiv preprint doi: https://doi.org/10.1101/2020.12.09.418657; this version posted December 10, 2020. The copyright holder for this preprint (which was not certified by peer review) is the author/funder, who has granted bioRxiv a license to display the preprint in perpetuity. It is made available under aCC-BY-NC-ND 4.0 International license.

testing of genetic and pharmacological approaches aimed at mitigating the consequences of Pol III-related leukodystrophy.

## Materials and Methods

### Animals

All experiments involving mice were performed using protocols approved by the Institutional Animal Care and Use Committee (IACUC) of the Albert Einstein College of Medicine. Mice were housed under standard laboratory conditions on a 12-hour light/dark cycle with constant access to food and water. The C57BL/6J-*Polr3a*$^{tm1Iwil}$ mouse line was generated by homologous recombination in C57BL/6J blastocysts (Ozgene Pty. Ltd.). This conditional *Polr3a* knock-in mouse (*Polr3a*$^{cKI/+}$) carries an insertion of a *Polr3a* cDNA encoding exons 15-31 and a downstream heterologous polyadenylation signal flanked by *loxP* sites followed by intronic sequences and a mutant exon 15 encoding the leukodystrophy mutations W671R and G672E. Cre-mediated recombination removes the wild-type cDNA to allow expression of the *Polr3a* mutant. Crosses of this mouse to one expressing a germline Cre recombinase were performed to generate mice heterozygous for the whole-body *Polr3a* knock-in (*Polr3a*$^{KI/+}$). B6.129-*Olig2*$^{tm1.1(cre)Wdr}$/J (*Olig2*Cre, stock number 025567) (50) mice and B6.129(Cg)-*Gt(ROSA)26Sor*$^{tm4(ACTB-tdTomato,-EGFP)Luo}$/J (tdTomato-EGFP, stock number 007676) (51) mice were purchased from the Jackson Laboratory. All experiments were performed with male and female mice except transmission electron microscopy (TEM) and western blots, which were performed using males.

### Developmental Milestones

The protocol from Hill et al. (28), was followed with two investigators participating in the execution and documentation of the tests (see SI Appendix). Briefly, prior to daily

bioRxiv preprint doi: https://doi.org/10.1101/2020.12.09.418657; this version posted December 10, 2020. The copyright holder for this preprint (which was not certified by peer review) is the author/funder, who has granted bioRxiv a license to display the preprint in perpetuity. It is made available under aCC-BY-NC-ND 4.0 International license.

testing, pups were removed from the home cage and placed with a small amount of nesting material on a heating pad set at 37°C. On P2, each mouse pup was weighed and given a unique tail tattoo mark. Tests were repeated daily until completed successfully on two consecutive days. The first day of passing each test is reported.

**Western Analysis**

All tissues were snap-frozen in liquid nitrogen immediately after harvesting. For POLR3A detection, whole brain samples were homogenized in RIPA lysis buffer supplemented with protease inhibitors (cOmplete mini + EDTA, Roche, 1 mM PMSF, 10 μg/ml leupeptin) and phosphatase inhibitors (10 mM sodium fluoride, 20 mM glycerophosphate-β , 2 mM sodium orthovanadate and 25 mM sodium pyrophosphate). Proteins were quantified by a bicinchoninic acid assay (Pierce). Protein (50 µg) was resolved by SDS-PAGE (6%) and transferred to nitrocellulose in 1X Tris-glycine buffer with 20% methanol. POLR3A and vinculin were detected by ECL (LAS-400, GE Healthcare) and quantified using ImageQuant software. Extracts from cerebrum and cerebellum were prepared by homogenization in Triton X-100 lysis buffer with protease inhibitors, as above and phosphatase inhibitors (Cocktails 2 and 3, Sigma). Proteins were quantified by Bradford assay (Biorad). Protein (50µg) was resolved by SDS-PAGE (12% gels for MOG, Caspase-3, CC1 and 8% gels for PDGFRα) and transferred to nitrocellulose using 1X Tris-glycine 0.1% SDS buffer with 15% ethanol using a semi-dry apparatus. Protein transfer (detected by Ponceau staining) and specific proteins detected by ECL (KwikQuant Imager) were quantified using Image J (NIH).

Antibodies and dilutions were: POLR3A (Abcam 96328; 1:750), Vinculin (Santa Cruz 73614; 1:2000), MOG (EMB MAB5680; 1:1000), CC1 (Abcam 16794; 1:1000), Caspase-3 (Cell Signaling 9662; 1:1000), PDGFRα (Cell Signaling 3174; 1:1000).

**RNA Analysis**

bioRxiv preprint doi: https://doi.org/10.1101/2020.12.09.418657; this version posted December 10, 2020. The copyright holder for this preprint (which was not certified by peer review) is the author/funder, who has granted bioRxiv a license to display the preprint in perpetuity. It is made available under aCC-BY-NC-ND 4.0 International license.

Tissue samples (50–100 mg, flash-frozen in liquid N2) were homogenized into Trizol lysis reagent (Thermo Fisher), and RNA was purified according to the manufacturer's directions. RNA was reprecipitated, quantified, and resolved by denaturing polyacrylamide electrophoresis before electrophoretic transfer to Nytran Plus membranes (GE Healthcare) and hybridization with [$^{32}$P]-end labeled oligonucleotide probes at 42°C or direct staining. Precursor tRNA$^{Ile}$(TAT) transcripts detected by phosphorimaging were quantified and normalized to U3 snRNA (52). Mature tRNAs visualized with ethidium bromide were quantified and normalized to 5.8S rRNA.

**Behavioral studies**

Behavioral studies were carried out by blinded operators on two separate cohorts of mice at 12 weeks of age. The tests included video monitoring and analysis in a Behavioral Spectrometer (BIOBSERVE), object placement and object recognition tests, Hargreaves, acoustic startle and tape removal tests, elevated plus maze, balance beam and rotarod (see SI Appendix).

**Immunohistochemistry**

Brain and spinal cord were harvested after isoflurane anesthesia and cardiac perfusion (4% paraformaldehyde, PFA) and were stored at 4°C in 4% PFA overnight before long-term storage in 25% sucrose. Frozen tissue was sectioned into 10 µm slices using a cryostat and stained with the BrainStain imaging kit (Invitrogen B3645) according to the manufacturer’s protocol. Paraffin-embedded tissue was sectioned into 15 µm slices for staining with LFB and Nissl, which followed standard procedures. Purkinje cell counts were performed as previously reported (53). For antibody staining, 5 µm sections of fully formed hippocampus and corpus callosum splenium regions were deparaffinized before heat-mediated antigen retrieval in citrate buffer. Blocking, primary and secondary antibody steps used 0.1% Triton X-100, 5% goat serum, 5% BSA in 1X TBS. Primary

bioRxiv preprint doi: https://doi.org/10.1101/2020.12.09.418657; this version posted December 10, 2020. The copyright holder for this preprint (which was not certified by peer review) is the author/funder, who has granted bioRxiv a license to display the preprint in perpetuity. It is made available under aCC-BY-NC-ND 4.0 International license.

antibodies and dilutions were: MBP (SMI99 EMD NE1019; 1:1000), MAG (Boster PA1751; 1:200) and CC1 (Calbiochem OP80 APC; 1:20). Secondary antibodies were either anti-mouse Alexa-Fluor 488 or anti-rabbit Alexa-Fluor 568 (1:1000 dilution). Slides were mounted with ProLong diamond antifade with DAPI (Invitrogen P36966) and images were acquired using a 3D Histech p250 high capacity slide scanner.

**Transmission Electron Microscopy**

Brains, harvested after anesthesia and sequential cardiac perfusion with 15 ml/mouse of 0.09% NaCl containing heparin (25 mg/ml) and 4% PFA in 0.1 M cacodylate buffer, were post-fixed in 2% PFA 2.5% glutaraldehyde in 0.1 M cacodylate buffer for 30 min at room temperature. A brain matrix was used to dissect the region encompassing the midline of the corpus callosum. 1-mm sections were oriented to generate cross-sections of axons within the corpus callosum. Ultrathin sections were cut and stained with toluidine blue. A minimum of 10 images that showed axons cut in cross-section were obtained at 5K, 10K and 20K magnification for quantitation. Images were analyzed by Photoshop software using the free hand selection tool and manually thresholded to determine the number of myelinated axons, axon size, myelin thickness and g-ratios. 300 axons/mouse were analyzed from 10 non-serial sections from 10K images. An axon was counted as unmyelinated if the area of the axon was equal to or larger than the area of the smallest myelinated axon in the corresponding field. Images were acquired on a JEOL 1200 EX transmission electron microscope.

**Flow Cytometry**

Following cardiac perfusion with ice-cold 1X PBS, the brain was harvested and cut into small pieces in a petri dish filled with PBS on ice. An adult brain dissociation kit (Miltenyi 130-107-67) was used to obtain a single cell suspension per the manufacturer's protocol. Briefly, tissues were dissociated mechanically and enzymatically followed by

bioRxiv preprint doi: https://doi.org/10.1101/2020.12.09.418657; this version posted December 10, 2020. The copyright holder for this preprint (which was not certified by peer review) is the author/funder, who has granted bioRxiv a license to display the preprint in perpetuity. It is made available under aCC-BY-NC-ND 4.0 International license.

debris and red blood cell removal steps. The cell suspension was passed through a 0.35 µm filter before staining with trypan blue to assess cell viability and determine cell counts. The suspension was centrifuged at 300xg for 10 min at 4°C and resuspended (up to $10^7$ cells) in 900 µl of FACS buffer (ice-cold 1X PBS). The suspension was blocked with 100 µl of FcR blocking reagent (Miltenyi 130-092-575) for 10 min on ice. Primary conjugated antibodies were diluted according to the manufacturer's protocol; O4 Alexa Fluor 647 (RND FAB1326R; 6µl/$10^6$ cells), mGalC-FITC (EMD FCMAB312F; 10µl/$10^6$ cells), MOG (EMD MAB5680; 10µl/$10^6$ cells) conjugated with a lightning-link PE-Cy7 tandem conjugation kit per the manufacturer's protocol (Novus 7620005). Primary antibodies were incubated on ice for 20 min in the dark, washed with 2 ml of FACS buffer, centrifuged at 350xg for 7 min at 4°C. The pellet was resuspended in 1 ml of FACS buffer and analysis was performed on a LSRII-U flow cytometer (BD Biosciences). Single color controls were used to determine proper gating prior to sample analysis.

**Magnetic resonance imaging (MRI)/Proton magnetic resonance spectroscopy ($^1$H MRS)**

All MRI and $^1$H MRS data were acquired in a 9.4 T Varian Direct Drive system (Agilent Technologies, Santa Clara, CA, USA). A 14 mm diameter receive-only surface RF coil (Doty Scientific, Columbia, SC, USA) along with a 7 cm ID $^1$H transmit and receive body coil (M2M Imaging, Cleveland, OH, USA) was used. Anesthesia was achieved with 1.25% isoflurane mixed with room air. Respiration was monitored with a pressure pad (SA Instruments, Stony Brook, NY, USA). Temperature was maintained at ~37°C using warm air with feedback from a thermocouple placed in the rectum (SA Instruments). Imaging parameters and details of the analyzes are provided in SI Appendix.

bioRxiv preprint doi: https://doi.org/10.1101/2020.12.09.418657; this version posted December 10, 2020. The copyright holder for this preprint (which was not certified by peer review) is the author/funder, who has granted bioRxiv a license to display the preprint in perpetuity. It is made available under aCC-BY-NC-ND 4.0 International license.

## Acknowledgments

This work was supported by National Institutes of Health grants RO1-GM120358 (to IMW) and R21-HD097557 (to IMW and RDM). Additional support was provided by the Rose F. Kennedy Intellectual and Developmental Disabilities Research Center (IDDRC), which is funded through a center grant from the Eunice Kennedy Shriver National Institute of Child Health & Human Development (NICHD U54-HD090260) and by an Albert Einstein Cancer Center core support grant (P30-CA013330). We thank David Spray for comments on the manuscript.

## References

1. W. Kohler, J. Curiel, A. Vanderver, Adulthood leukodystrophies. *Nat Rev Neurol* **14**, 94-105 (2018).
2. M. S. van der Knaap, M. Bugiani, Leukodystrophies: a proposed classification system based on pathological changes and pathogenetic mechanisms. *Acta Neuropathologica* **134**, 351-382 (2017).
3. H. E. Soderholm, A. B. Chapin, P. Bayrak-Toydemir, J. L. Bonkowsky, Elevated Leukodystrophy Incidence Predicted From Genomics Databases. *Pediatr Neurol* **111**, 66-69 (2020).
4. G. Bernard *et al.*, Mutations of POLR3A encoding a catalytic subunit of RNA polymerase Pol III cause a recessive hypomyelinating leukodystrophy. *Am J Hum Genet* **89**, 415-423 (2011).
5. M. Tetreault *et al.*, Recessive mutations in POLR3B, encoding the second largest subunit of Pol III, cause a rare hypomyelinating leukodystrophy. *Am J Hum Genet* **89**, 652-655 (2011).
6. H. Saitsu *et al.*, Mutations in POLR3A and POLR3B encoding RNA Polymerase III subunits cause an autosomal-recessive hypomyelinating leukoencephalopathy. *Am J Hum Genet* **89**, 644-651 (2011).
7. H. Daoud *et al.*, Mutations in POLR3A and POLR3B are a major cause of hypomyelinating leukodystrophies with or without dental abnormalities and/or hypogonadotropic hypogonadism. *J Med Genet* **50**, 194-197 (2013).
8. N. I. Wolf *et al.*, Clinical spectrum of 4H leukodystrophy caused by POLR3A and POLR3B mutations. *Neurology* **83**, 1898-1905 (2014).
9. M. R. Richards *et al.*, Phenotypic spectrum of POLR3B mutations: isolated hypogonadotropic hypogonadism without neurological or dental anomalies. *J Med Genet* **54**, 19-25 (2017).
10. E. A. Verberne, L. Dalen Meurs, N. I. Wolf, M. M. van Haelst, 4H leukodystrophy caused by a homozygous POLR3B mutation: Further delineation of the phenotype. *Am J Med Genet A* **182**, 1776-1779 (2020).

bioRxiv preprint doi: https://doi.org/10.1101/2020.12.09.418657; this version posted December 10, 2020. The copyright holder for this preprint (which was not certified by peer review) is the author/funder, who has granted bioRxiv a license to display the preprint in perpetuity. It is made available under aCC-BY-NC-ND 4.0 International license.


11. M. S. van der Knaap, R. Schiffmann, F. Mochel, N. I. Wolf, Diagnosis, prognosis, and treatment of leukodystrophies. *The Lancet. Neurology* **18**, 962-972 (2019).
12. R. D. Moir, I. M. Willis, Regulation of pol III transcription by nutrient and stress signaling pathways. *Biochim Biophys Acta* **1829**, 361-375 (2013).
13. M. Yeganeh, N. Hernandez, RNA polymerase III transcription as a disease factor. *Genes Dev* **34**, 865-882 (2020).
14. G. Dieci, A. Conti, A. Pagano, D. Carnevali, Identification of RNA polymerase III-transcribed genes in eukaryotic genomes. *Biochim Biophys Acta* **1829**, 296-305 (2013).
15. I. Thiffault *et al.*, Recessive mutations in POLR1C cause a leukodystrophy by impairing biogenesis of RNA polymerase III. *Nat Commun* **6**, 7623 (2015).
16. I. Dorboz *et al.*, Mutation in POLR3K causes hypomyelinating leukodystrophy and abnormal ribosomal RNA regulation. *Neurology. Genetics* **4**, e289 (2018).
17. P. A. Terhal *et al.*, Biallelic variants in POLR3GL cause endosteal hyperostosis and oligodontia. *Eur J Hum Genet* **28**, 31-39 (2020).
18. M. Girbig *et al.*, Cryo-EM structures of human RNA polymerase III in its unbound and transcribing states. *bioRxiv* 10.1101/2020.06.29.177642, 2020.2006.2029.177642 (2020).
19. E. P. Ramsay *et al.*, Structure of human RNA Polymerase III. *bioRxiv* 10.1101/2020.06.29.177279, 2020.2006.2029.177279 (2020).
20. D. N. Azmanov *et al.*, Transcriptome-wide effects of a POLR3A gene mutation in patients with an unusual phenotype of striatal involvement. *Hum Mol Genet* **25**, 4302-4314 (2016).
21. K. Choquet *et al.*, Leukodystrophy-associated POLR3A mutations down-regulate the RNA polymerase III transcript and important regulatory RNA BC200. *J Biol Chem* **294**, 7445-7459 (2019).
22. K. Choquet *et al.*, Absence of neurological abnormalities in mice homozygous for the Polr3a G672E hypomyelinating leukodystrophy mutation. *Mol Brain* **10**, 13 (2017).
23. K. Choquet *et al.*, The leukodystrophy mutation Polr3b R103H causes homozygote mouse embryonic lethality and impairs RNA polymerase III biogenesis. *Mol Brain* **12**, 59 (2019).
24. R. D. Moir, C. Lavados, J. Lee, I. M. Willis, Functional characterization of Polr3a hypomyelinating leukodystrophy mutations in the *S. cerevisiae* homolog, RPC160. *Gene* 10.1016/j.gene.2020.145259, 145259 (2020).
25. J. Ju *et al.*, Olig2 regulates Purkinje cell generation in the early developing mouse cerebellum. *Sci Rep* **6**, 30711 (2016).
26. D. H. Meijer *et al.*, Separated at birth? The functional and molecular divergence of OLIG1 and OLIG2. *Nat Rev Neurosci* **13**, 819-831 (2012).
27. K. Tatsumi *et al.*, Olig2-Lineage Astrocytes: A Distinct Subtype of Astrocytes That Differs from GFAP Astrocytes. *Front Neuroanat* **12**, 8 (2018).
28. J. M. Hill, M. A. Lim, M. M. Stone, "Developmental Milestones in the Newborn Mouse" in Neuropeptide Techniques, I. Gozes, Ed. (Humana Press, Totowa, NJ, 2008), 10.1007/978-1-60327-099-1_10, pp. 131-149.
29. J. J. Tuscher, A. M. Fortress, J. Kim, K. M. Frick, Regulation of object recognition and object placement by ovarian sex steroid hormones. *Behavioural brain research* **285**, 140-157 (2015).

bioRxiv preprint doi: https://doi.org/10.1101/2020.12.09.418657; this version posted December 10, 2020. The copyright holder for this preprint (which was not certified by peer review) is the author/funder, who has granted bioRxiv a license to display the preprint in perpetuity. It is made available under aCC-BY-NC-ND 4.0 International license.

30. M. E. Shenton *et al.*, A review of magnetic resonance imaging and diffusion tensor imaging findings in mild traumatic brain injury. *Brain Imaging Behav* **6**, 137-192 (2012).
31. A. L. Alexander, J. E. Lee, M. Lazar, A. S. Field, Diffusion tensor imaging of the brain. *Neurotherapeutics* **4**, 316-329 (2007).
32. S. K. Song *et al.*, Dysmyelination revealed through MRI as increased radial (but unchanged axial) diffusion of water. *NeuroImage* **17**, 1429-1436 (2002).
33. M. Renner *et al.*, Optic Nerve Degeneration after Retinal Ischemia/Reperfusion in a Rodent Model. *Frontiers in cellular neuroscience* **11**, 254-254 (2017).
34. M. Assadi, D.-J. Wang, Y. Velazquez-Rodriquez, P. Leone, Multi-Voxel 1H-MRS in Metachromatic Leukodystrophy. *J Cent Nerv Syst Dis* **5**, 25-30 (2013).
35. B. Kruse *et al.*, Alterations of brain metabolites in metachromatic leukodystrophy as detected by localized proton magnetic resonance spectroscopy in vivo. *Journal of neurology* **241**, 68-74 (1993).
36. K. Brockmann *et al.*, Proton MRS profile of cerebral metabolic abnormalities in Krabbe disease. *Neurology* **60**, 819-825 (2003).
37. M. C. Judson *et al.*, Decreased Axon Caliber Underlies Loss of Fiber Tract Integrity, Disproportional Reductions in White Matter Volume, and Microcephaly in Angelman Syndrome Model Mice. *The Journal of Neuroscience* **37**, 7347-7361 (2017).
38. N. Snaidero, M. Simons, Myelination at a glance. *J Cell Sci* **127**, 2999-3004 (2014).
39. D. E. Bergles, W. D. Richardson, Oligodendrocyte Development and Plasticity. *Cold Spring Harb Perspect Biol* **8**, a020453 (2015).
40. A. P. Robinson, J. M. Rodgers, G. E. Goings, S. D. Miller, Characterization of oligodendroglial populations in mouse demyelinating disease using flow cytometry: clues for MS pathogenesis. *PLoS One* **9**, e107649 (2014).
41. L. O. Sun *et al.*, Spatiotemporal Control of CNS Myelination by Oligodendrocyte Programmed Cell Death through the TFEB-PUMA Axis. *Cell* **175**, 1811-1826 e1821 (2018).
42. M. D'Amelio, M. Sheng, F. Cecconi, Caspase-3 in the central nervous system: beyond apoptosis. *Trends Neurosci* **35**, 700-709 (2012).
43. D. Liko *et al.*, Brf1 loss and not overexpression disrupts tissues homeostasis in the intestine, liver and pancreas. *Cell Death & Differentiation* **26**, 2535-2550 (2019).
44. X. Wang, A. Gerber, W. Y. Chen, R. G. Roeder, Functions of paralogous RNA polymerase III subunits POLR3G and POLR3GL in mouse development. *Proceedings of the National Academy of Sciences of the United States of America* **117**, 15702-15711 (2020).
45. F. Pelletier *et al.*, Endocrine and Growth Abnormalities in 4H Leukodystrophy Caused by Variants in POLR3A, POLR3B, and POLR1C. *J Clin Endocrinol Metab* 10.1210/clinem/dgaa700 (2020).
46. K. B. Smedlund, J. W. Hill, The role of non-neuronal cells in hypogonadotropic hypogonadism. *Molecular and cellular endocrinology* 10.1016/j.mce.2020.110996, 110996 (2020).
47. R. E. Pepper, K. A. Pitman, C. L. Cullen, K. M. Young, How Do Cells of the Oligodendrocyte Lineage Affect Neuronal Circuits to Influence Motor Function, Memory and Mood? *Frontiers in Cellular Neuroscience* **12** (2018).

bioRxiv preprint doi: https://doi.org/10.1101/2020.12.09.418657; this version posted December 10, 2020. The copyright holder for this preprint (which was not certified by peer review) is the author/funder, who has granted bioRxiv a license to display the preprint in perpetuity. It is made available under aCC-BY-NC-ND 4.0 International license.

48. N. Camargo *et al.*, Oligodendroglial myelination requires astrocyte-derived lipids. *PLoS biology* **15**, e1002605-e1002605 (2017).
49. C. Y. Chen *et al.*, Maf1 and Repression of RNA Polymerase III-Mediated Transcription Drive Adipocyte Differentiation. *Cell Rep* **24**, 1852-1864 (2018).
50. M. Zawadzka *et al.*, CNS-resident glial progenitor/stem cells produce Schwann cells as well as oligodendrocytes during repair of CNS demyelination. *Cell Stem Cell* **6**, 578-590 (2010).
51. M. D. Muzumdar, B. Tasic, K. Miyamichi, L. Li, L. Luo, A global double-fluorescent Cre reporter mouse. *Genesis* **45**, 593-605 (2007).
52. N. Bonhoure *et al.*, Loss of the RNA polymerase III repressor MAF1 confers obesity resistance. *Genes Dev* **29**, 934-947 (2015).
53. M. Girard *et al.*, Mitochondrial dysfunction and Purkinje cell loss in autosomal recessive spastic ataxia of Charlevoix-Saguenay (ARSACS). *Proceedings of the National Academy of Sciences of the United States of America* **109**, 1661-1666 (2012).

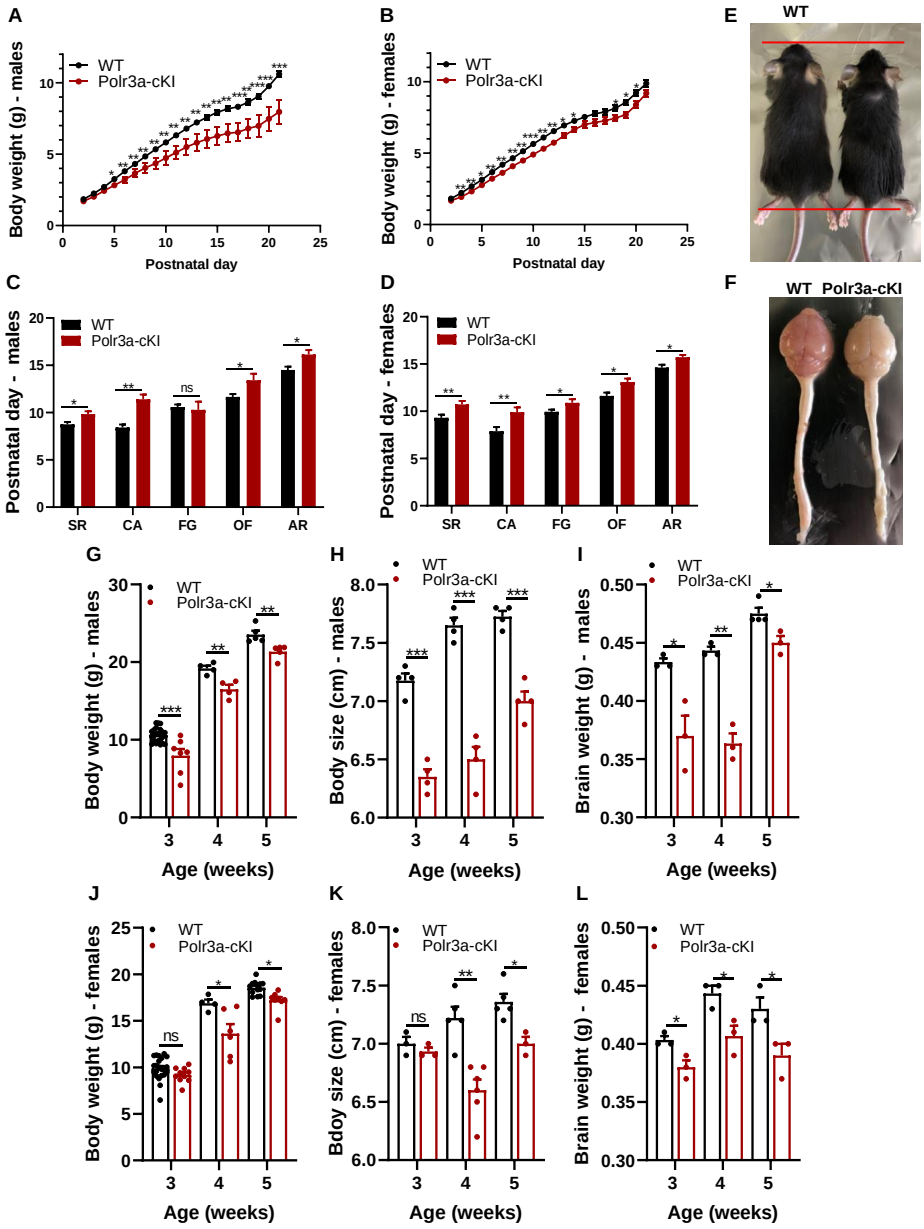


**Fig. 1.** Body metrics and developmental milestone assessment of neonates and adolescent WT and Polr3a-cKI mice. (A) Neonate male body weight curves (WT n=22, Polr3a-cKI n=7, nested t test p=0.0011). (B) Neonate female body weight curves (WT n=22, Polr3a-cKI n=10, nested t test p=0.01). (C) Male developmental milestones (WT n=20 (SR, OF and AR), 19 (CA) and 17 (FG); Polr3a-cKI n=6 (SR, FG, OF and AR) and 5 (FG); nested t test p=0.0061). (D) Female developmental milestones (WT n=19 (SR, OF and AR), 18 (CA) and 17 (FG); Polr3a-cKI n=11 (SR, CA, OF and AR), 9 (FG); nested t test p=0.0028). SR: surface righting; CA: cliff aversion; FG: forelimb grasp; OF: open field; AR: air righting. For A-D, the same mice were analyzed at multiple data points or tests (repeated measures). (E) Image of WT and Polr3a-cKI mice highlighting the body size difference at 3 weeks of age. (F) Image of WT and Polr3a-cKI brain and spinal cord. (G-I) Body weight, body size and brain weight of WT and Polr3a-cKI adolescent males, respectively. (J-L) Body weight, body size and brain weight of WT and Polr3a-cKI adolescent females, respectively. Values are presented as the mean ± SEM. Groups were compared using two-sided Student's t-test at each time point (multiple t test), *<0.05, **<0.01, ***<0.001.

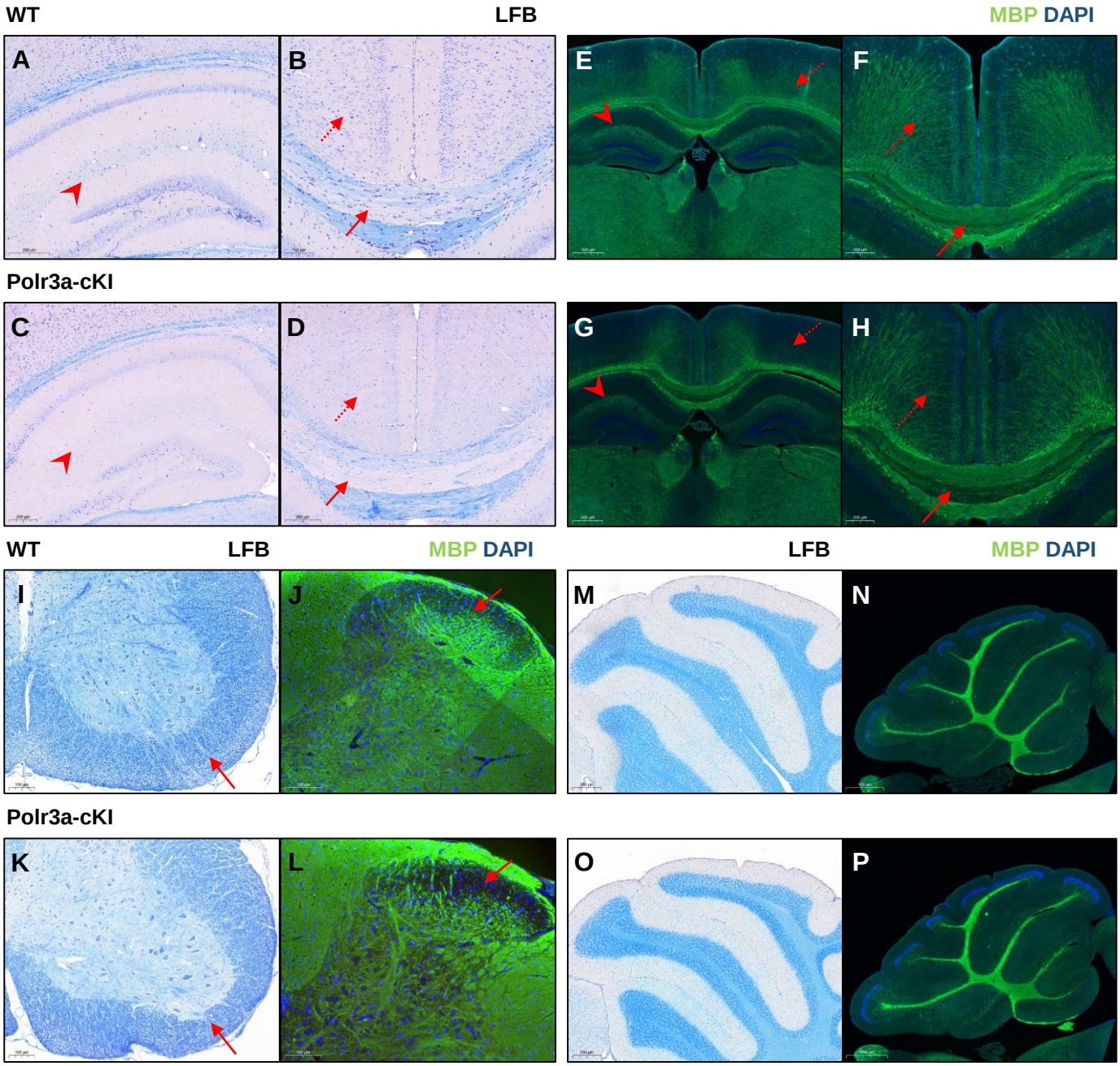


**Fig. 2.** Immunohistochemical staining of cerebral, cerebellar and spinal cord sections from adolescent WT and Polr3a-cKI mice. (A-D) LFB staining of the hippocampus (arrowhead), corpus callosum splenium (solid arrow) and the cortex (dashed arrow). (E-H) MBP staining of the hippocampus (arrowhead), corpus callosum splenium (solid arrow) and cortex (dashed arrow). (I and K) LFB staining of spinal cord sections (solid arrow highlights differences in the ventral horn). (J and L) MBP staining of the spinal cord (solid arrow highlights differences in the dorsal horn). (M and O) LFB staining of cerebellar sagittal sections. (N and P) MBP staining of cerebellar sagittal sections. Images are representative of 3 mice/condition/sex.

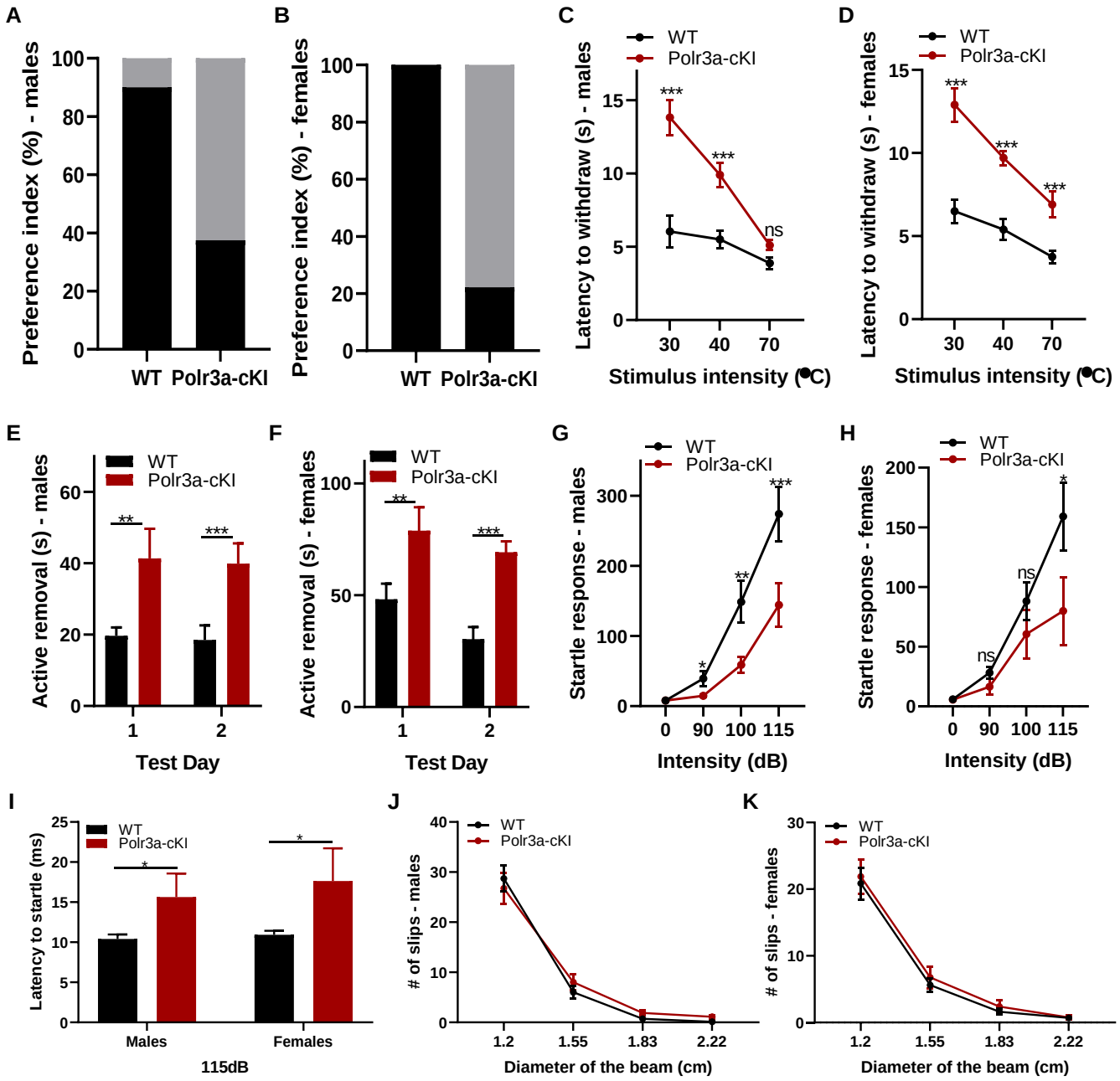


**Fig. 3.** Behavioral testing of adult WT and Polr3a-cKI mice reveals cognitive, sensory and fine sensorimotor deficits. (A and B) Cognitive assessment of object placement for males and females. Data are plotted as the percentage of animals that achieve a preference score >55 (black bar, animals scoring above the cutoff) and those that fail to reach this cutoff, i.e. no preference (gray bar, Chi-square test for both sexes $p<0.001$). (C and D) Hargreaves test for males and females. The latency for hind paw withdrawal is plotted as a function of stimulus intensity. (E and F) Tape removal test for males and females. The time of active tape removal is reported for tests performed on consecutive days. (G and H) Acoustic startle test for males and females. The startle reflex (mV per gram body weight) is reported as a function of stimulus intensity. (I) Acoustic startle latency at a stimulus intensity of 115dB (one-way ANOVA for each sex; both sexes $p<0.05$). (J and K) Balance beam reporting the number of slips from 4 different beams ranging from hard (1.2 cm) to easy (2.22 cm) for males and females respectively (repeated measures ANOVA $p>0.85$).

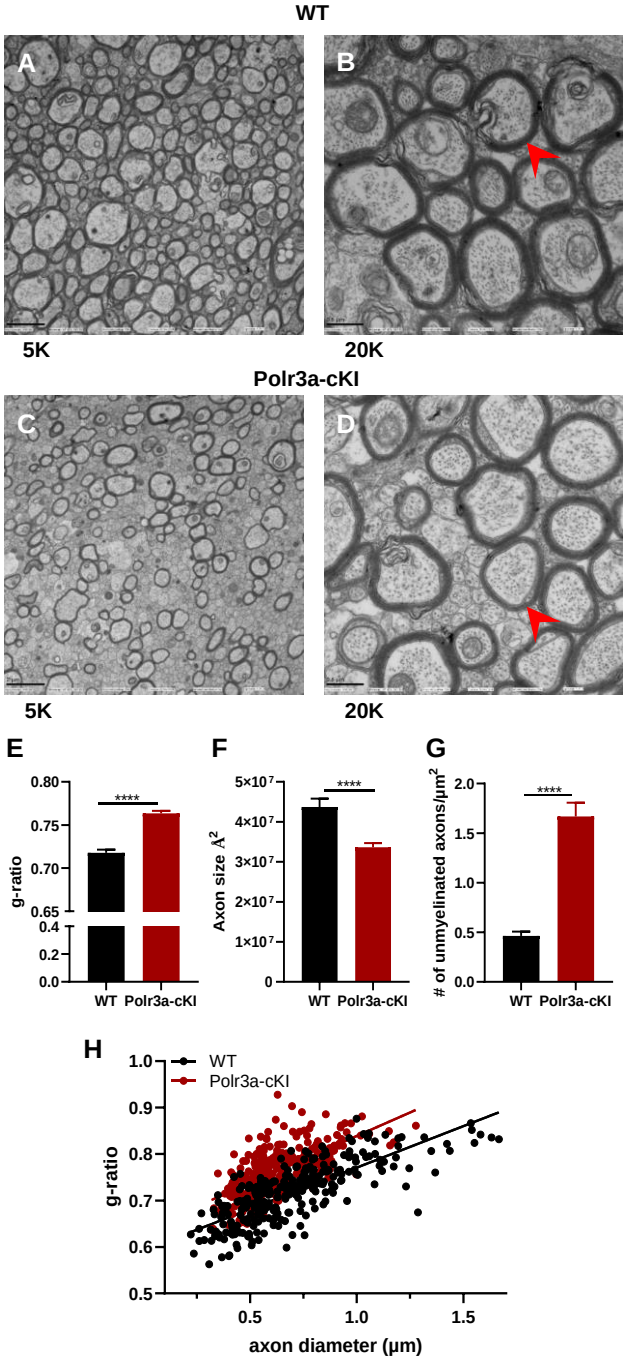


**Fig. 4.** TEM images of the corpus callosum in adult male mice. (A-B) Representative WT images at 5K & 20K magnification, respectively. (C-D) Representative Polr3a-cKI images at 5K & 20K respectively. Arrowhead highlights differences in myelin thickness for axons of similar size. (E) Average g-ratio (radius of axon/radius of axon+myelin), n=300/group. (F) Axon size reported as axon area without myelin, n=300/group. (G) Number of unmyelinated axons/µm2, n=10 fields/group. An axon is counted as unmyelinated if the area of the axon is equal to or larger than the smallest myelinated axon in the corresponding WT field. (H) g-ratio as a function of axon diameter, n=300/group; comparison of fits for linear regression, y-intercept comparison between conditions (p<0.0001****). Quantitation was performed on 10 independent images/group at 10K magnification. Values are presented as the mean ± SEM. Groups were compared using two-sided Student's t-test unless otherwise indicated, ****p<0.0001.

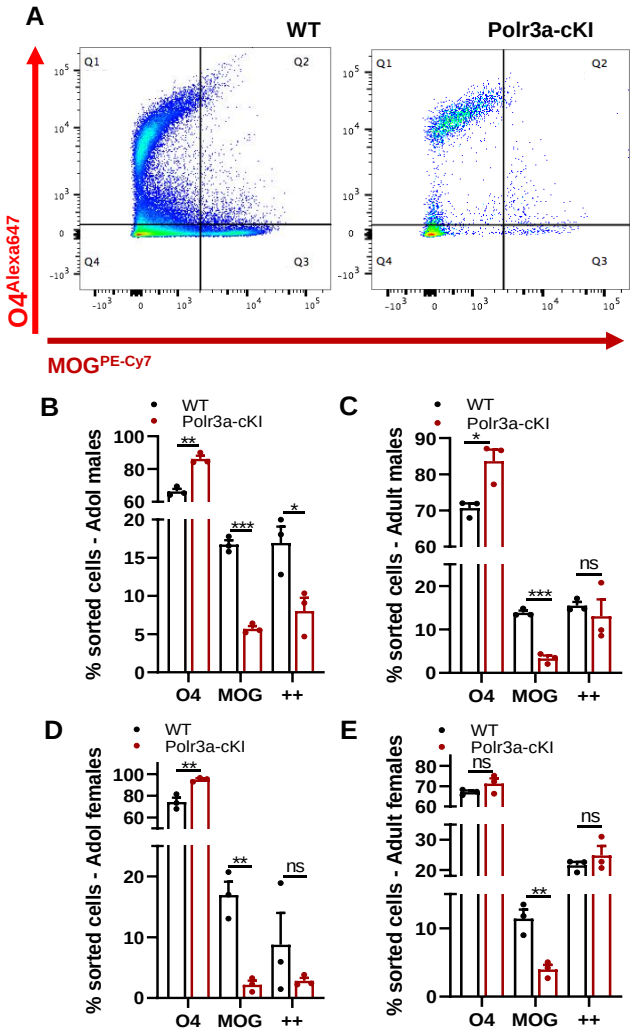


**Fig. 5.** Flow cytometry of oligodendrocyte cell populations from WT & Polr3a-cKI mice. (A) Representative scatter plots from flow cytometry show gating of O4, MOG & double-positive oligodendrocytes in whole brain from adolescent female mice. (B and D) Quantitation of O4, MOG & double positive (++) oligodendrocytes in adolescent male and female samples. (C and E) Quantitation of O4, MOG & double positive (++) oligodendrocytes in adult male and female samples. EGFP-expressing cells in Polr3a-cKI samples were gated so that only oligodendrocyte lineage cells that had undergone Cre-mediated recombination would be counted. Values are presented as the mean ± SEM. Groups of n=3 mice/condition/sex were compared using multiple t tests, *p<0.05, **p<0.01, ***p<0.001.

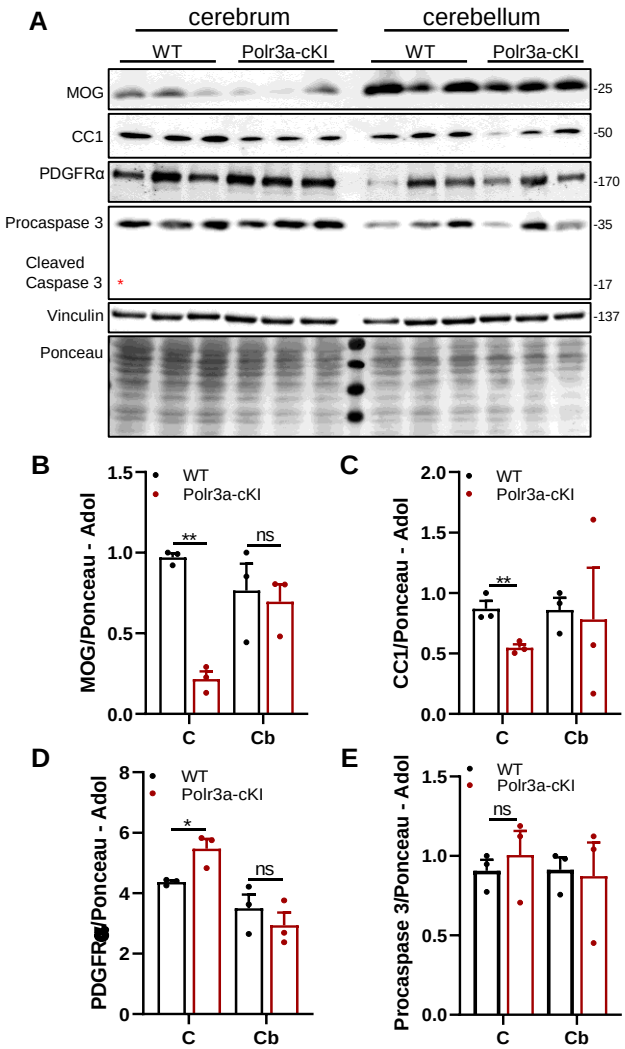


**Fig. 6.** Western blot analysis of cerebrum (C) and cerebellum (Cb) extracts from adolescent male mice. (A) Representative blots are shown for MOG, CC1, PDGFRα, pro- and cleaved caspase 3 and vinculin along with a Ponceau S-stained membrane. Red asterisk indicates the absence of cleaved caspase 3. (B-E) Quantitation of the indicated proteins was normalized using the Ponceau S signal. Values are presented as the mean ± SEM. Groups of n=3 mice/condition were compared using multiple t tests, *p<0.05, **p<0.01, ***p<0.001.

bioRxiv preprint doi: https://doi.org/10.1101/2020.12.09.418657; this version posted December 10, 2020. The copyright holder for this preprint (which was not certified by peer review) is the author/funder, who has granted bioRxiv a license to display the preprint in perpetuity. It is made available under aCC-BY-NC-ND 4.0 International license.

**Table 1. Magnetic Resonance Imaging (MRI) T1 and T2 relaxation times of different brain regions*.**

| Structure | T1 (s) | T2 (ms) |
|---|---|---|
| **Corpus callosum - Genu** | | |
| WT | 1.84 ± 0.22 | 34.5 ± 2.1 |
| Pol3ra-cKI | 1.88 ± 0.14 | 37.5 ± 2.7 |
| p | 0.72 | 0.038 |
| **Corpus callosum - Splenium** | | |
| WT | 1.69 ± 0.06 | 34.7 ± 1.7 |
| Pol3ra-cKI | 1.72 ± 0.06 | 38.7 ± 1.9 |
| p | 0.46 | 0.0014 |
| **Cortex** | | |
| WT | 1.83 ± 0.03 | 43.9 ± 3.2 |
| Polr3a-cKI | 1.86 ± 0.03 | 45.7 ± 3.0 |
| p | 0.06 | 0.32 |
| **Hippocampus** | | |
| WT | 1.86 ± 0.03 | 45.7 ± 2.8 |
| Polr3a-cKI | 1.87 ± 0.05 | 46.8 ± 2.7 |
| p | 0.71 | 0.44 |

* All values are presented as the mean ± SD, combining data from males and females n = 7.

bioRxiv preprint doi: https://doi.org/10.1101/2020.12.09.418657; this version posted December 10, 2020. The copyright holder for this preprint (which was not certified by peer review) is the author/funder, who has granted bioRxiv a license to display the preprint in perpetuity. It is made available under aCC-BY-NC-ND 4.0 International license.

**Table 2. Diffusion Tensor Imaging of different brain regions***.

| Structure | FA | MD | AD | RD |
|---|---|---|---|---|
| **Anterior commissure** | | | | |
| WT | 0.64 ± 0.04 | 0.64 ± 0.03 | 1.18 ± 0.06 | 0.36 ± 0.03 |
| Polr3a-cKI | 0.59 ± 0.04 | 0.66 ± 0.03 | 1.17 ± 0.05 | 0.41 ± 0.03 |
| p | 0.044 | 0.134 | 0.729 | 0.017 |
| **Optic nerve** | | | | |
| WT | 0.88 ± 0.06 | 0.78 ± 0.10 | 1.79 ± 0.09 | 0.27 ± 0.11 |
| Polr3a-cKI | 0.89 ± 0.03 | 0.62 ± 0.03 | 1.54 ± 0.08 | 0.16 ± 0.04 |
| p | 0.848 | 0.043 | 0.0002 | 0.035 |
| **Corpus callosum - Genu** | | | | |
| WT | 0.65 ± 0.03 | 0.75 ± 0.09 | 1.33 ± 0.08 | 0.42 ± 0.07 |
| Polr3a-cKI | 0.58 ± 0.05 | 0.76 ± 0.06 | 1.31 ± 0.05 | 0.48 ± 0.08 |
| p | 0.009 | 0.880 | 0.631 | 0.161 |
| **Corpus callosum - Splenium** | | | | |
| WT | 0.77 ± 0.03 | 0.66 ± 0.03 | 1.39 ± 0.09 | 0.28 ± 0.02 |
| Polr3a-cKI | 0.70 ± 0.06 | 0.67 ± 0.01 | 1.32 ± 0.09 | 0.34 ± 0.06 |
| p | 0.024 | 0.352 | 0.137 | 0.017 |
| **Optic tract** | | | | |
| WT | 0.78 ± 0.04 | 0.65 ± 0.07 | 1.34 ± 0.09 | 0.26 ± 0.02 |
| Polr3a-cKI | 0.73 ± 0.03 | 0.64 ± 0.02 | 1.30 ± 0.04 | 0.31 ± 0.03 |
| p | 0.0244 | 0.598 | 0.337 | 0.0071 |

* Fractional anisotropy (FA), mean diffusivity (MD), axial diffusivity (AD), radial diffusivity (RD); values for MD, AD & RD are $10^{-5}$ $cm^2$/sec. All values are presented as the mean ± SD, combining data from males and females n = 7.